

# Dynamically tunable polarized mid-infrared light-emitting diodes from polarization singularities in a band-edge Weyl node

Received: 4 July 2025

Accepted: 29 October 2025

Published online: 12 December 2025

 Check for updates

Junrong Zhang<sup>1,2,8</sup>, Fengyuan Xuan<sup>3,8</sup>, Jiexi Song<sup>3,8</sup>, Junsheng Xu<sup>1,4</sup>, Dong Wang<sup>1,4</sup>, Quanlong Zhang<sup>1,4</sup>, Qinghua Han<sup>1,4</sup>, Keyu Cheng<sup>1,4</sup>, Yaning Liang<sup>1,5</sup>, Xingang Hou<sup>1</sup>, Xiangyi Wang<sup>1,4</sup>, Jing Xu<sup>1</sup>, Yuan Gan<sup>1,4</sup>, Xicheng Yang<sup>1,4</sup>, Bingyan Ren<sup>6</sup>, Weijie Zhao<sup>6,7</sup>, Junyong Wang<sup>1,2,4</sup> ✉ & Kai Zhang<sup>1,2,4</sup> ✉

The polarization states of light-emitting devices in conventional semiconductors are typically deterministically fixed by optical transition selection rules. However, in emerging Weyl semiconductors, band-crossing Weyl nodes introduce exotic polarization contrasts, making emission polarization sensitive to carrier dynamics. Here, we demonstrate mid-infrared light-emitting diodes based on van der Waals tellurium, a Weyl semiconductor featuring a Weyl node precisely at the conduction band minimum (CBM). These devices demonstrate high polarization tunability, with linear polarization degrees continuously adjustable from -100% (low carrier density) to 36% (high carrier density). First-principles calculations reveal that this tunability originates from polarization singularities induced by CBM-located Weyl nodes, where the polarization state is dynamically modulated by the quasi-Fermi level shift and hot-carrier recombination under varying injection densities. Our findings establish band-edge Weyl nodes as a promising platform for tunable polarized emitters and open alternative avenues for topological optoelectronics.

Polarization is a fundamental degree of freedom in light-emitting devices, encoding information essential for optical communication, signal encryption, and quantum computing<sup>1–3</sup>. The polarization state of luminescence depends on the emitter's symmetry and the density of electromagnetic modes permitted by the optical environment. In a semiconducting light-emitting diode (LED), polarization is governed by transition matrix elements (determined by the crystal symmetry of the semiconductor) and band-edge electron states, which follow optically allowed transitions with specific selection rules<sup>4–6</sup>. While device integration with engineered nanostructures can further modify

polarization<sup>7,8</sup>, conventionally fabricated devices exhibit fixed polarization states. An on-chip, miniaturized LED capable of dynamic polarization tuning would be transformative for photonic applications but remains elusive.

Band-crossing electronic states in emerging quantum materials give rise to exotic phenomena—including strongly correlated phases<sup>9</sup>, excitonic insulators<sup>10</sup>, and topological Dirac/Weyl nodes<sup>11</sup>—that can fundamentally alter light-matter interactions. For instance, Weyl semimetals/semiconductors exhibit unique polarization responses near their band-crossing topological nodes<sup>12,13</sup>. However, the Weyl

<sup>1</sup>i-Lab, Suzhou Institute of Nano-Tech and Nano-Bionics (SINANO), Chinese Academy of Sciences, Suzhou, Jiangsu, China. <sup>2</sup>Key Laboratory of Semiconductor Display Materials and Chips, Suzhou Institute of Nano-Tech and Nano-Bionics (SINANO), Chinese Academy of Sciences, Suzhou, Jiangsu, China. <sup>3</sup>Suzhou Laboratory, Suzhou, China. <sup>4</sup>School of Nano-Tech and Nano-Bionics, University of Science and Technology of China, Hefei, Anhui, China. <sup>5</sup>School of Materials Science and Engineering, Shanghai University, Shanghai, China. <sup>6</sup>School of Physics, Frontiers Science Center for Mobile Information Communication and Security, Southeast University, Nanjing, Jiangsu, China. <sup>7</sup>Purple Mountain Laboratories, Nanjing, Jiangsu, China. <sup>8</sup>These authors contributed equally: Junrong Zhang, Fengyuan Xuan, Jiexi Song. ✉ e-mail: [jywang2022@sinano.ac.cn](mailto:jywang2022@sinano.ac.cn); [kzhang2015@sinano.ac.cn](mailto:kzhang2015@sinano.ac.cn)

nodes currently manifest themselves primarily in electrical transport (require precise Fermi-level tuning<sup>14–16</sup>) or ultrafast spectroscopy (probe a superposition of absorption responses from multiple bands)<sup>13,17,18</sup>, leaving their potential for polarization-tunable light emission unexplored. This gap can be addressed by the emerging 2D Weyl semiconductor tellurium (Te)<sup>19–24</sup>, where low crystal symmetry and strong spin-orbit coupling position Weyl nodes (W3) precisely at the band edge<sup>25–27</sup>, allowing direct coupling between the topological band crossing point and carrier recombination<sup>28,29</sup>. The distinctive properties establish 2D Te as a prototypical material for dynamically tunable polarized emitters, distinct from the approximated parabolic dispersion band edge in conventional semiconductors<sup>12,13,18,29,30</sup>.

In this work, we demonstrate dynamic polarization modulation in Te via band-edge recombination mediated by Weyl nodes. By constructing van der Waals (vdW) heterojunction mid-infrared (MIR) LEDs capable of operating across a broad carrier injection range, we reveal a unique polarization-tuning mechanism absent in conventional semiconducting emitters. The atomically sharp interface and extended transition distribution in the reciprocal space for carriers in 2D Te enable efficient hot carrier injection and recombination under high injection regimes. Strikingly, the degree of linear polarization (DOP) exhibits current-density-dependent tuning, from nearly 100% at low current densities ( $-17 \mu\text{A}/\mu\text{m}^2$ ) to 36% at high densities ( $-105 \mu\text{A}/\mu\text{m}^2$ ). We attribute this behavior to a polarization singularity arising from the Weyl-node-mediated band crossing at the conduction band minimum (CBM), where topological band structure directly governs radiative recombination. This work establishes 2D Te as a prototype for band-edge Weyl semiconducting light emitters, opening alternative avenues to explore light-matter interactions at Weyl points and develop tunable topological optoelectronic devices operating in the MIR regime.

## Results

### Polarized MIR light emission from 2D Te with Weyl node in the CBM

Quasi-1D Te consists of helical chains stacked in hexagonal arrays via vdW forces, with each chain (aligned along the z-axis) comprising a repeating unit of three Te atoms (Fig. 1a). High-quality Te nanosheets were synthesized via chemical vapor deposition (CVD) (see “Methods”). These nanosheets exhibit remarkable stability, which was confirmed by Raman spectroscopy and atomic force microscopy (AFM) (Fig. 1b), and possess topological characteristics that make them promising for competitive optoelectronic applications<sup>14,17,19,31</sup>. Notably, the three Raman-active modes ( $E_1$  TO at  $92 \text{ cm}^{-1}$ ,  $A_1$  at  $121 \text{ cm}^{-1}$ , and  $E_2$  at  $141 \text{ cm}^{-1}$ ) and AFM profiles remain virtually unchanged after two months (Fig. 1b, Supplementary Fig. 1). Angle-resolved polarized Raman spectroscopy further reveals strong in-plane anisotropy and crystallographic orientation (Supplementary Fig. 2). High-resolution spherical aberration-corrected scanning transmission electron microscopy (STEM) images, shown in Fig. 1c (in-plane) and 1d (cross-sectional), confirm the high crystallinity of the samples.

The MIR light emission properties of Te nanosheets were investigated by using a home-built infrared micro-photoluminescence (micro-PL) system (see “Methods”, and Supplementary Fig. 3). Figure 1e displays the power-dependent PL spectra of a Te nanosheet measured at room temperature. As the laser power density increases from  $0.16 \mu\text{W}/\mu\text{m}^2$  to  $1.44 \mu\text{W}/\mu\text{m}^2$ , the PL peak intensity increases linearly, as shown in the inset of Fig. 1e, ruling out emission contributions from localized states. As the thickness decreases from 589 nm to 45 nm, the emission energy slightly increases within the range of 0.35–0.36 eV (see Supplementary Fig. 4). The emission from thicker flakes aligns with the bandgap and optical absorption of bulk Te<sup>23,32,33</sup>. Te samples with different thicknesses all exhibit good linear polarization characteristics under low excitation power (see

Supplementary Fig. 5). Additionally, temperature-dependent bandgap modulation arises from lattice thermal expansion and electron-lattice interactions (Supplementary Fig. 6). Notably, the Te nanosheets possess comparable PL efficiency to the typical 2D MIR emitter material black phosphorus (BP) at room temperature with a higher air stability<sup>34,35</sup> (Supplementary Fig. 7).

The band structure of Te with spin-orbit coupling (SOC) effects is depicted in Fig. 1f. As a result of mirror symmetry breaking, the non-magnetic chiral Te crystal has Kramers-Weyl points that are protected by T-symmetry at time-reversal invariant points, such as the CBM at H point in the Brillouin zone (BZ), and the so-called double Kramers-Weyl points protected by the combination of  $T$  and  $C_{3i}$  screw rotation symmetry<sup>36</sup>. Unlike accidental Weyl points arising from symmetry breaking, the Kramers-Weyl point at the CBM (H point) is inherently robust and should not be affected by minor impurities or lattice distortions<sup>37</sup>. These double Kramers-Weyl points may suppress non-radiative recombination through topological protection<sup>38</sup>, while the large Berry curvature dipole near the Weyl nodes modulates electron-hole recombination matrix elements<sup>31</sup>. This unique mechanism suggests that Te could enable unconventional tunable LEDs. It is worth noting that our theoretical calculations (Fig. 1g) predict a reduction in the DOP due to PL spectral broadening; the trend is consistent with the polarization PL modulation observed in Te (Supplementary Fig. 8). Electro-injection MIR devices offer a promising approach for exploiting the band-edge transition of Te (centered at the H point, Fig. 1h inset) via direct charge carrier injection from vdW heterostructures<sup>39</sup>. Under high current injection, the polarization contribution along the z-axis increases, while the contribution along the x-axis diminishes (Fig. 1h). The schematic diagram shows the decreasing trend of the linear polarization degree under a large injection current density. This aligns with theoretical predictions (Fig. 1g) and the polarization-tunable PL (Supplementary Fig. 9), presents a viable strategy for actively controlling LED polarization.

### Tunable polarized MIR emission from band crossing in Te

To probe light emission properties across different injection current regimes, we employed the thin-layer graphene (Gr) to construct a Gr/Te/Gr heterostructure LED with low parasitic resistance and enable a broad range of injection currents. The top Gr ( $\text{Gr}_T$ ) and bottom Gr ( $\text{Gr}_B$ ) with different thicknesses were designed to sandwich the Te flake and function as a hole and electron injection layer to the Te, respectively (see “Methods” for details). Since Te exhibits  $p$ -doping, we design the thinner layer Gr as an electron injection layer since its Fermi level is more readily tunable via bias voltage. Figure 2a shows a schematic of the heterostructure and its band alignment, while Supplementary Fig. 10 displays an optical micrograph of the device (junction area  $\sim 60.5 \mu\text{m}^2$ ). Figure 2b, c presents bias-dependent electroluminescence (EL) alongside the PL spectrum, confirming that EL originates from band-edge recombination rather than thermal emission. EL intensity increases with both forward and reverse biases, yet exhibits asymmetric turn-on thresholds of  $-2.8 \text{ V}$  (reverse) and  $4.0 \text{ V}$  (forward). The reverse bias induces faster EL growth and higher brightness, a consequence of the optimized Gr thickness asymmetry. Figure 2d illustrates the EL intensity and current density  $j_d$  versus bias voltage  $V_d$ . Enhanced electron injection efficiency through a thinner layer of graphene under reverse bias boosts the EL intensity, yielding a quantum efficiency of 2.18% at a reverse current density  $j_d$  of  $-52.06 \mu\text{A}/\mu\text{m}^2$ , surpassing forward-bias performance (Supplementary Note 1, Figs. 11–14). It is worth noting that the current density  $j_d$  in the  $\text{Gr}_T/\text{Te}/\text{Gr}_B$  heterojunction spans two orders of magnitude, covering broad current injection regimes.

Bias-dependent EL spectra (Fig. 2e) and their normalized profiles (Fig. 2f) reveal significant spectral modifications under increasing

reverse bias. The observed blue shift and spectral broadening emerge from enhanced carrier injection at high voltages, where the combined effects of band-filling and non-equilibrium Fermi-Dirac distributions redistribute electronic transitions from the band edge through hot carrier generation in reciprocal space. This interpretation is further supported by the development of a high-energy tail in the spectra,

which serves as a direct indicator of elevated effective carrier temperatures under high current densities. The frequency dependence of the emission spectrum can be described using the Eq. (1)<sup>40–42</sup>:

$$I(h\nu) \propto (h\nu - E_g)^{\frac{1}{2}} \exp\left(-\frac{h\nu - E_g}{k_B T}\right) \quad (1)$$

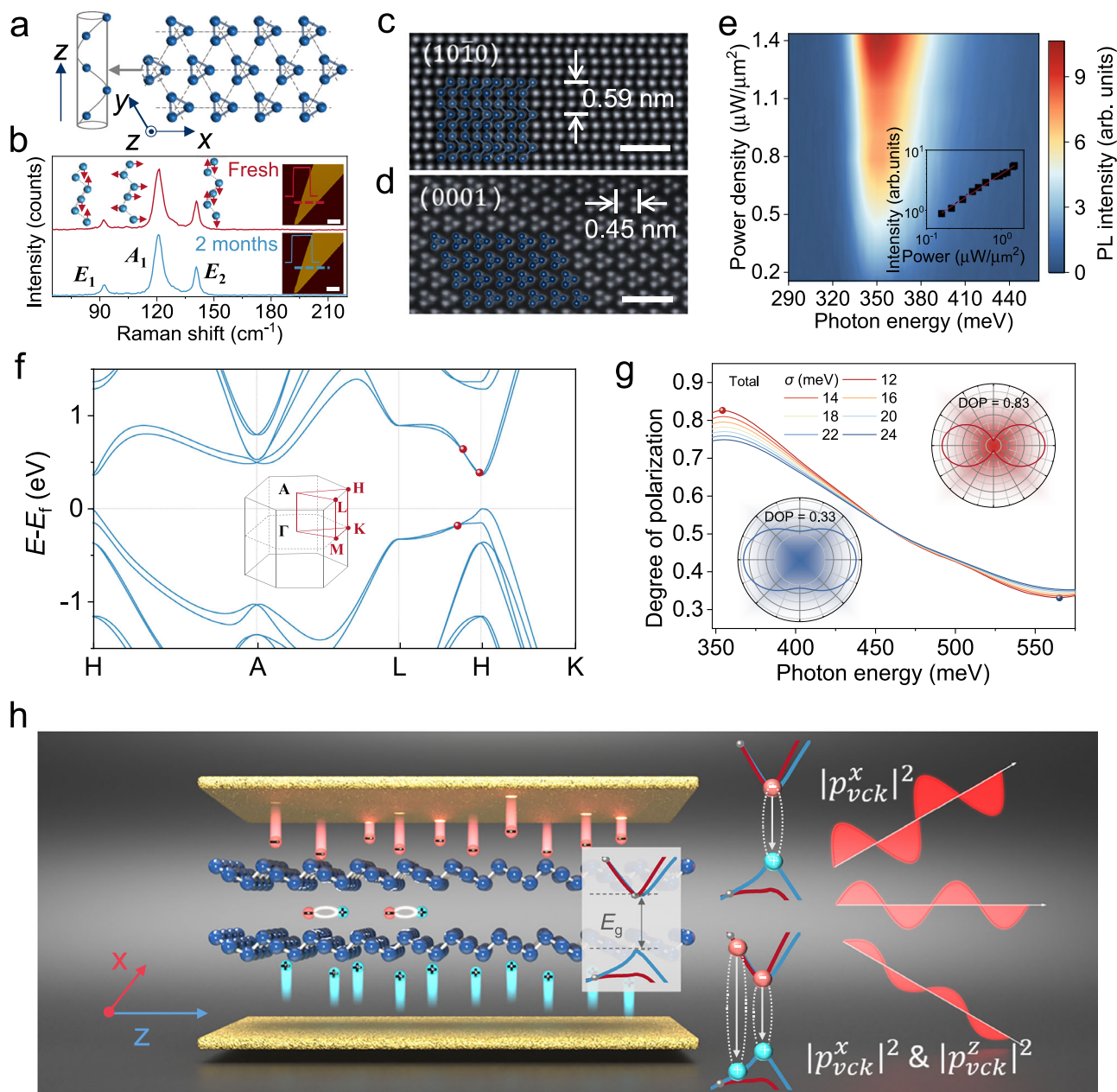


**Fig. 1 | Polarized mid-infrared (MIR) light emission from 2D Te with Weyl node in the conduction band minimum (CBM).** **a** Crystal structure of Te, a single chain is shown in the left panel, and the right panel shows the view of the Te crystal structure along the z-axis (chain direction). **b** Ambient-stable Raman spectra of Te nanosheet. Inset shows the atomic force microscope (AFM) images of a freshly prepared Te nanosheet (Scale bar: 5 μm) and after 2 months of air exposure (Scale bar: 5 μm), demonstrating environmental stability. **c, d** In-plane ((c), Scale bar: 1 nm) and cross-sectional ((d), Scale bar: 1 nm) high-resolution scanning transmission electron microscopy (STEM) images of Te nanosheets. **e** Power-dependent photoluminescence (PL) intensity of a Te nanosheet. The inset is the relationship between PL intensity and pump power density. **f** The density functional theory (DFT)-calculated band structure of Te near the H point in the first Brillouin zone

(BZ). Inset: First BZ of Te.  $E_f$ : the Fermi level. **g** Calculated degree of polarization (DOP) as a function of peak broadening. The insets show polar plots corresponding to DOPs of 0.83 (high polarization) and 0.33 (low polarization).  $\sigma$ : broadening parameter to quantify the peak broadening effect. **h** The schematic diagram of the electrically-driven Te-based light-emitting diode (LED). The x and z directions are the orthogonal directions of the Te chain and the direction of the Te chain, respectively. The upper and lower electrodes inject electrons and holes into the Te, respectively, and the radiative recombination occurs within the Te. The dotted lines represent the electron-hole pairs, and the arrows indicate their recombination. The transition intensity along the x and z directions are represented by  $|p_{vck}^x|^2$  and  $|p_{vck}^z|^2$ , respectively.  $E_g$ : the bandgap of Te.

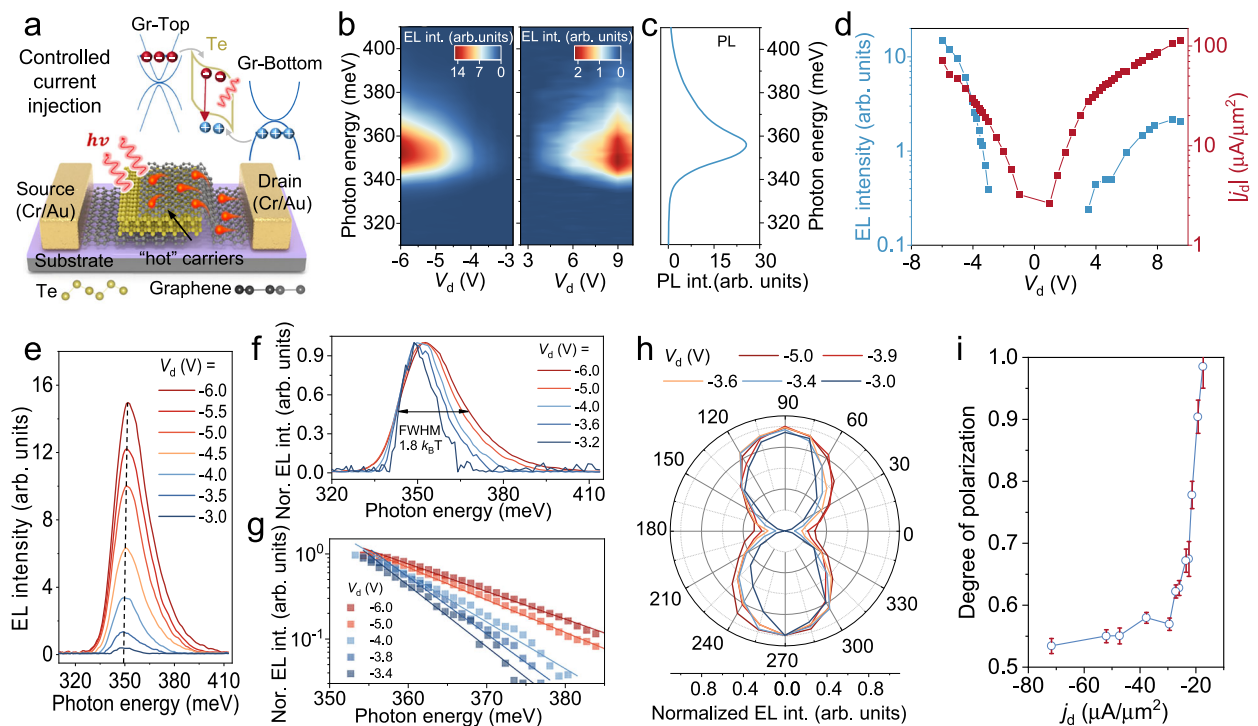


**Fig. 2 | Tunable polarized MIR emission from band crossing in Te.** **a** The schematic illustration of the Gr<sub>Top</sub>/Te/Gr<sub>Bottom</sub> heterostructure LED. Band diagram of Gr<sub>Top</sub>/Te/Gr<sub>Bottom</sub> under operational bias.  $h\nu$ : The energy of emitted photons. **b** Contour maps of electroluminescence (EL) spectra as a function of reverse bias and forward bias at 78 K. **c** The corresponding PL spectrum of Te in Gr<sub>Top</sub>/Te/Gr<sub>Bottom</sub> heterostructure. **d** Semi-logarithmic plot of EL intensity (blue) and current density  $j_d$  (red) as a function of bias voltage  $V_d$ . **e** Bias-dependent EL spectra. **f** Normalized EL spectra of Gr<sub>Top</sub>/Te/Gr<sub>Bottom</sub> at different  $V_d$ . FWHM: Full width at half maximum.  $k_B$ : Boltzmann

constant.  $T$ : Temperature. **g** Semi-log plots of normalized EL intensity versus photon energy. The lines are linear fits to the corresponding data. **h** Polar plot of the normalized EL intensity at different  $V_d$ , demonstrating polarization tunability. **i** DOP of Gr<sub>Top</sub>/Te/Gr<sub>Bottom</sub> LED as a function of  $j_d$ . The error bars indicate the standard deviation of the DOP, obtained from three independent measurements of EL intensity and calculated using the error propagation formula for DOP =  $(|p_{vck}^x|^2 - |p_{vck}^z|^2) / (|p_{vck}^x|^2 + |p_{vck}^z|^2)$ .

where,  $I$  is the luminescence intensity,  $h\nu$  is the photon energy,  $E_g$  is the band gap,  $k_B$  is the Boltzmann constant, and  $T$  is the temperature of carriers. According to the equation, the EL spectrum rises sharply at energy near  $E_g$  due to the factor  $\sqrt{(h\nu - E_g)}$  and then falls off exponentially with a decay constant of  $k_B T$  due to the Boltzmann factor  $\exp(-\frac{h\nu - E_g}{k_B T})$ , and the linewidth is approximately proportional to  $k_B T$ . By analyzing both the slope of the semi-logarithmic EL intensity versus photon energy plot (Fig. 2g) and the spectral linewidth (Fig. 2f), we quantitatively determine that the effective carrier temperature rises from 80 K to 155 K with increasing current density (Supplementary Fig. 15), establishing a clear relationship between carrier thermalization and injection level<sup>41–43</sup>. The ultrafast transient reflection spectroscopy measurements further verify that Te supports a much slower carrier relaxation, which is favorable for hot-carrier recombination (“Methods”, Supplementary Fig. 16). These observations collectively demonstrate efficient hot carrier injection and recombination processes under high-current conditions. Importantly, these hot carriers fundamentally modify the polarization characteristics of the emission. While low current densities maintain near-perfect DOP (~100%) along the  $x$ -axis (90° and 270°), increasing current injection leads to significant DOP reduction as the injected carrier density increases (Fig. 2h). Figure 2i reveals that the DOP along the  $x$ -axis (90° and 270°) decreases from nearly 100% to 53% with rising current density, with forward bias conditions driving the DOP even lower to 36% (Supplementary Fig. 17). The reproducibility of this electrically tunable DOP behavior in additional Gr<sub>Top</sub>/Te/Gr<sub>Bottom</sub> LED devices (Supplementary Figs. 18–21) confirms the universal nature of this current-driven polarization modulation effect, providing compelling evidence for

hot carrier-mediated control over emission properties. Furthermore, a Gr<sub>Top</sub>/Te/Au device was also constructed to ensure that this tunable DOP behavior originated from the intrinsic properties of Te (Supplementary Fig. 22). This constitutes a dynamically reconfigurable MIR light emission device through simple current injection modulation.

### Origin of dynamically tunable polarized MIR emission

The photoexcitation and light emission of Te were measured in the (10 $\bar{1}$ 0) plane, corresponding to the  $x$ - $z$  plane (Fig. 3a). The fundamental electron-hole transitions occur at the H point in the BZ. Increasing carrier injection shifts carrier filling from H toward L, A, and K directions of the Te BZ (Fig. 3b, c) and an averaged effect from the optical transition in the BZ around the H point will lead to the change of DOP. To elucidate the dependence of polarization on bias voltage observed in the EL experiment, we analyzed the optical transition strength  $|p_{vck}^2| = |(vk|p|ck)|^2$  in a small region near H point (Supplementary Note 2). With minimal  $k_z$ -dependence of  $|p_{vck}^2|$  (Detailed discussion is presented in Supplementary Figs. 23, 24), we focus on the results at the  $k_z = 0.5$  plane. At the H point, optical transitions are dominated by  $|p_{vck}^x|^2$  (Fig. 3d, e), corresponding to the emission at CBM in the low current injection regime (Fig. 2i). The magnitude of  $|p_{vck}^z|^2$  increases with photon energy (the iso-gap contours shown in Supplementary Fig. 25) across broader regions of the BZ under high current injection. When the carriers are filled along the HA and HL directions, the polarization state of luminescence in the  $z$ -axis direction gradually increases, as shown in Fig. 3f, which together with the polarization state of luminescence in the orthogonal direction of the  $z$ -axis affects the DOP of light emission (Supplementary Fig. 26). The  $k$ -resolved DOP

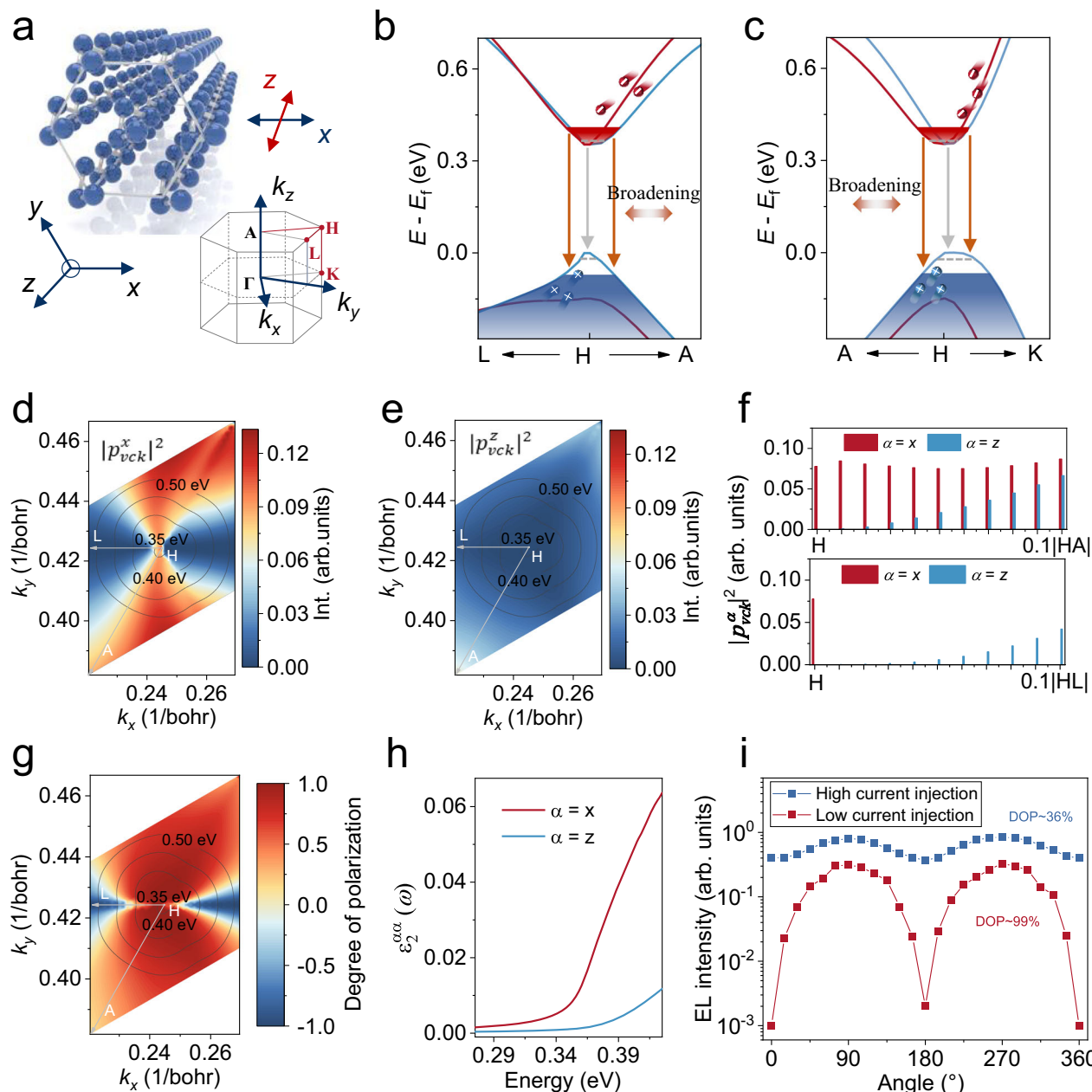


**Fig. 3 | Origin of dynamically tunable polarized MIR emission.** **a** Atomic structure of Te and high-symmetry points in its BZ.  $k_x$ ,  $k_y$  and  $k_z$  are the wave vector components in reciprocal space. **b**, **c** Zoomed-in band structure near the H point, highlighting the Weyl node at the conduction band minimum. The gray and orange arrows represent the radiative recombination of electron-hole pairs at the band

edges and away from the band edges, respectively. **d**, **e** Optical transition strength plot at  $k_z = 0.5$  around a small region near H. The contour curves are iso-gap lines. **f** The  $|p_{vck}|^2$  along the H-A and H-L paths. **g**  $k$ -resolved DOP plot at  $k_z = 0.5$  around a small region near H. The contour curves are iso-gap lines. **h** Calculated imaginary part of dielectric function  $\epsilon_2^{\alpha\alpha}(\omega)$ . **i** Semi-logarithmic plots of the polarized EL.

in a larger area of BZ can be obtained based on the optical transition strength by the formula  $DOP = (|p_{vck}^x|^2 - |p_{vck}^z|^2) / (|p_{vck}^x|^2 + |p_{vck}^z|^2)$ , as shown in Fig. 3g. It can be observed that the proximity of the H point exhibits as a polarization singularity due to the Weyl nodes ( $W_3$ ) in the CBM. A deviation from the H point would diverge the polarization sharply as a result of the band crossing at the Weyl node. Under band-filling conditions, the EL spectra exhibit broadening dominated by high-energy luminescence, while the reduction in polarization directly corresponds to the enhancement of  $|p_{vck}^z|^2$ , thereby corroborating our experimental observations. Additionally, we observe abrupt oscillator strength variations at another Weyl point along HL (Supplementary Fig. 27), further confirming the mediation of polarization from Weyl nodes.

The plot of the imaginary part of the dielectric function  $\epsilon_2^{\alpha\alpha}(\omega)$  versus photon energy indicates the transition intensities along the  $z$ -axis contribute significantly to the overall transition with the increase of photon energy (Fig. 3h). We use the broadening parameter ( $\sigma$ ) to quantize the peak broadening effect under different bias voltages in our theoretical calculation of  $\epsilon_2^{\alpha\alpha}(\omega)$  (Fig. 2f, Supplementary Table 1). Systematic examination of the DOP as a function of photon energy under different  $\sigma$  (Supplementary Fig. 28) demonstrates that the DOP diminishes with rising effective carrier temperature, consistent with thermal broadening suppressing the anisotropy of  $|p_{vck}^x|^2$ -dominated transitions. It is worth noting that the experimental polarization (Fig. 3i) decreases significantly, exceeds the calculated trend, indicating that non-equilibrium hot carrier injection beyond simple thermal

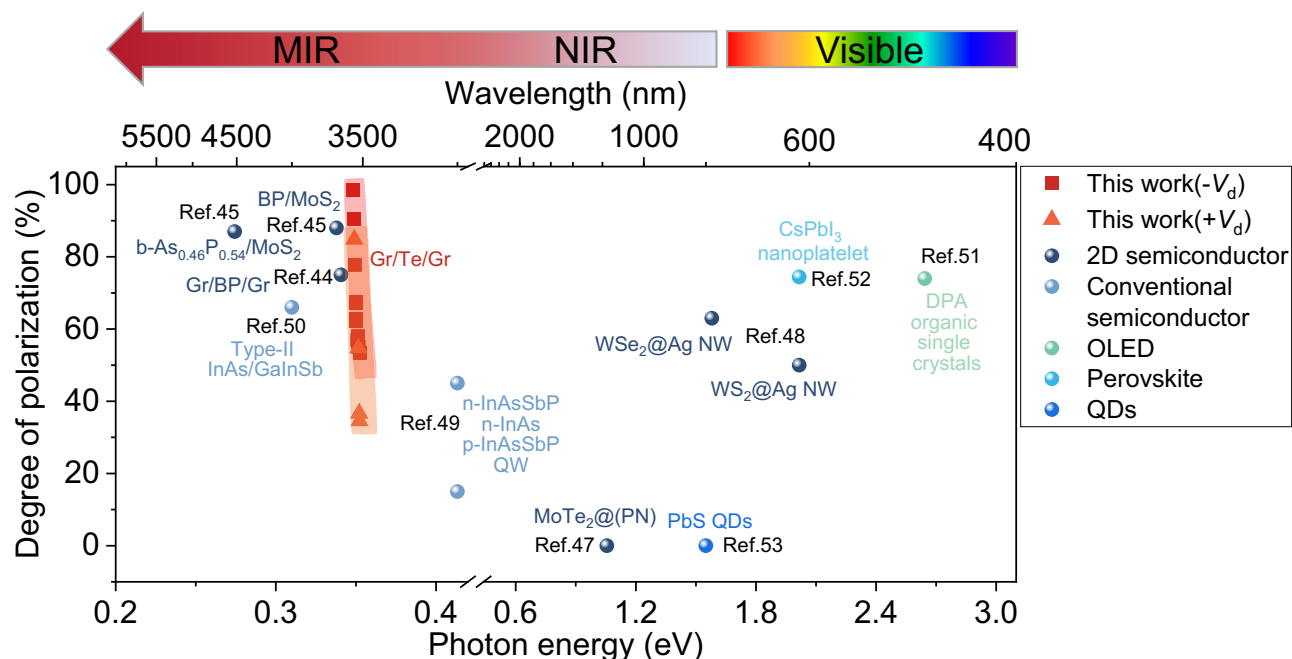


**Fig. 4 | Benchmark of the EL DOP of typical LEDs with various photon energies.** LEDs based on Te show a dynamically tunable broad DOP compared to other devices, including typical 2D semiconductors, III-V semiconductors, organic semiconductors, perovskite, and quantum dots.

effects plays a significant role in governing EL characteristics of Te. The extra decrease of DOP with rising current density, as shown in Supplementary Fig. 17 can be attributed to the non-equilibrium carrier distribution, which is located in the Brillouin Zone with significant  $|p_{vck}^z|^2$  contribution (see Supplementary Note 3, Fig. 29).

#### Comparison of the DOP of LEDs with different photon energies

Figure 4 presents a comprehensive benchmark comparing the DOP across typical LED technologies, including 2D semiconductors, III-V semiconductors, organic semiconductors, CsPbX<sub>3</sub> perovskites, and quantum dots (QDs), spanning visible to infrared wavelengths (see Supplementary Table 2 for details). Among 2D semiconductors, anisotropic BP<sup>44</sup> and its alloys<sup>45</sup>, commonly used as gain media in mid-infrared LEDs, exhibit strong linear polarization. However, unlike Te, BP's transitions at high-symmetry points in the BZ show fixed polarization along the armchair direction due to optical selection rules, with no sensitivity to external excitation<sup>44,46</sup>. LEDs based on transition metal chalcogenides typically emit light with negligible polarization due to the high crystal symmetry<sup>47</sup>, and a fixed polarization can only be achieved by coupling with the external structure<sup>48</sup>. Conventional III-V semiconductor LEDs<sup>49,50</sup> and emerging materials, such as organic semiconductors<sup>51</sup>, perovskites<sup>52</sup>, and quantum dots<sup>53</sup> (QDs), demonstrate polarization only within a fixed degree determined by the crystal symmetry and out-coupling structures. In contrast, Te-based LEDs exhibit unique polarization characteristics, where carrier density enables continuous and dynamic tuning of the DOP from 100% to 36%. The tunable polarization performance of Te-LEDs stems from their unique band structure, where carrier injection dynamically modulates the relative contributions of transitions corresponding to different polarized photons near the H point in the BZ. A defining characteristic of Kramers-Weyl points at the H point in tellurium is their robustness against perturbations that preserve both time-reversal symmetry and the specific point-group symmetries of the crystal lattice. This robustness stems from the topological protection conferred by these symmetries, guaranteeing the stability of the band crossing as long as the protecting symmetries remain intact<sup>37,54,55</sup>. This intrinsic mechanism enables polarization tunability, establishing Te-based devices as a platform for dynamically reconfigurable polarized light sources.

#### Discussion

We have demonstrated electrically tunable polarized EL in narrow-bandgap Te through carrier injection modulation. By leveraging the stable MIR light emission of Te nanosheets, LEDs based on Gr<sub>T</sub>/Te/Gr<sub>B</sub> heterojunction structure were constructed with an external quantum efficiency around 2.18%. These devices exhibit continuously adjustable linear polarization, with the DOP dynamically tunable from nearly 100% to 36% through current control. This tunability originates from band-filling effects near the H point in the first BZ and the consequent redistribution of electronic transitions in reciprocal space. The electrical control of polarization stems from hot carrier recombination near the band-crossing Weyl nodes at the CBM, where the evident polarization singularity enables this tunability. Our work demonstrates a polarization-tunable light source based on the polarization singularity in a band-edge Weyl node, providing an alternative platform for studying the interaction between the topological bands and emitting photons, and paving the way for exploiting innovative optoelectronic devices.

#### Methods

##### Tellurium flake synthesis

High-quality 2D Te flakes were synthesized by the hydrogen-assisted chemical vapor deposition under ambient pressure. Tellurium oxide power (TeO<sub>2</sub>, 99.99%, Aladdin) was placed in a quartz boat at the center of a single-zone tube furnace as a precursor, and mica was placed downstream as a growth substrate. The growth process was initiated by purging the system with high-purity argon (Ar, 200 sccm) for 5 min. The temperature was then raised to 560 °C under an Ar flow (60 sccm), followed by further heating to 700 °C with the introduction of hydrogen (H<sub>2</sub>, 20 sccm). After a 10-min dwell time, the furnace was cooled naturally to room temperature.

##### Material characterizations

The morphology of Te flakes was characterized using an optical microscope (Nikon, Eclipse L200N). The thicknesses of Te and Gr nanoflakes were identified via an atomic force microscope (Dimension ICON, Bruker). Raman scattering measurements were carried out by a Horiba LabRAM HR Evolution Raman confocal system with an

excitation photon energy of 2.33 eV through a 100× objective lens. Polarization-resolved Raman spectra were performed in the same Raman system by rotating the sample with respect to the excitation laser polarization. The atomic structure of Te were depicted via high-resolution scanning transmission electron microscopy (STEM, operating at 300 kV, Thermo Scientific, Themis Z). To study cross-sectional HR-STEM, the sample was fabricated by a standard focused ion beam (FEI Scios, FIB) fabrication process.

### Fabrication of Te LEDs and characterizations

For the vertically stacked Gr<sub>T</sub>/Te/Gr<sub>B</sub> heterostructure, Gr<sub>B</sub> (Few-layer Graphene) was prepared on SiO<sub>2</sub>/Si substrate by the standard mechanical exfoliation method, then a probe tip-assisted transfer approach was used to put the Te flake onto Gr<sub>B</sub>. Finally, Gr<sub>T</sub> was transferred on top with the PDMS-assisted dry transfer technique. Both heterojunctions are further heated at a temperature of 180 °C with a carrier gas of Argon (100 sccm) for 2 h to enhance van der Waals contacts and remove surface adsorbates. Cr/Au electrodes (10/120 nm) were deposited via electron-beam lithography and evaporation. Electrical characterization was performed using a Keysight B1500A semiconductor analyzer.

### Optical measurement

A home-built micro-PL system with an Er-doped femtosecond laser ( $\lambda = 1600$  nm, 80 MHz, 50 fs) was used for steady-state mid-infrared PL measurements. Emission was collected via a 15× mid-infrared (MIR) reflective objective and analyzed using a Horiba iHR 320 spectrometer with a liquid-nitrogen-cooled InSb detector (1–5.4  $\mu\text{m}$ ). Signal-to-noise ratios were enhanced using a lock-in amplifier (Stanford Research Systems SR830). For EL measurements of Te-based devices, the devices were driven by DC voltages generated from Keithley 2400 source meters with the same setup used in the PL measurement. Polarization-resolved MIR PL and EL were measured by placing a mid-infrared linear polarizer in front of the spectrometer. A continuous flow cryostat (Scryo-S-500, PHYSIKE) was used to control the temperatures.

### Micro-resolved pump-probe reflectance spectroscopy

The ultrafast transient reflection spectroscopy measurements are conducted by employing a commercial transient absorption spectrometer (TA 100, *Time-Tech Spectra*, China). The 1030 nm output pulse laser (100 kHz repetition rate, ~200 fs pulse width) from a femtosecond Yb: KGW laser (Pharos, *Light Conversion*) is split into two paths. One beam goes through a mechanical delay stage to pump nonlinear crystals to generate a light continuum to serve as the probe pulse. The second beam is sent to an optical parametric amplifier (Orpheus, *Light Conversion*) to generate pump pulses. The pump and probe pulses are collinearly focused on samples with a beam size of about 20 and 5  $\mu\text{m}$ , respectively, by using a 100× Olympus objective. A mechanical chopper with a synchronized readout of a CMOS detector is used for acquisitions of probe spectra with and without pump-induced changes, enabling the measurement of a differential reflectance. For each transient reflection spectrum, multi-scans are performed to ensure the repeatability of the obtained results.

### Data availability

The Source Data underlying the figures of this study are available with the paper. All raw data generated during the current study are available from the corresponding authors upon request. Source data are provided with this paper.

### References

1. N-Damask, J. *Polarization Optics in Telecommunications*. (Springer Science & Business Media, 2004).
2. Wang, Y. et al. Efficient quantum memory for single-photon polarization qubits. *Nat. Photonics* **13**, 346–351 (2019).
3. Crespi, A. et al. Integrated photonic quantum gates for polarization qubits. *Nat. Commun.* **2**, 566 (2011).
4. Huard, S. *Polarization of Light*. (Wiley-VCH, Chichester, 1997).
5. Wang, Y. et al. Polarization-dependent selection rules and optical spectrum Atlas of twisted bilayer graphene quantum dots. *Phys. Rev. X* **12**, 021055 (2022).
6. Gardner, N. F., Kim, J. C., Wierer, J. J., Shen, Y. C. & Krames, M. R. Polarization anisotropy in the electroluminescence of *m*-plane InGaN–GaN multiple-quantum-well light-emitting diodes. *Appl. Phys. Lett.* **86**, 111101 (2005).
7. Matioli, E. et al. High-brightness polarized light-emitting diodes. *Light.: Sci. Appl.* **1**, e22 (2012).
8. Deng, J. et al. An on-chip full-Stokes polarimeter based on optoelectronic polarization eigenvectors. *Nat. Electron.* **7**, 1004–1014 (2024).
9. Shen, C. et al. Dirac spectroscopy of strongly correlated phases in twisted trilayer graphene. *Nat. Mater.* **22**, 316–321 (2022).
10. Varsano, D., Palumbo, M., Molinari, E. & Rontani, M. A monolayer transition-metal dichalcogenide as a topological excitonic insulator. *Nat. Nanotechnol.* **15**, 367–372 (2020).
11. Lv, B. Q., Qian, T. & Ding, H. Experimental perspective on three-dimensional topological semimetals. *Rev. Mod. Phys.* **93**, 025002 (2021).
12. Guo, C., Asadchy, V. S., Zhao, B. & Fan, S. Light control with Weyl semimetals. *eLight* **3**, 2 (2023).
13. Ma, Q., Krishna Kumar, R., Xu, S.-Y., Koppens, F. H. L. & Song, J. C. W. Photocurrent as a multiphysics diagnostic of quantum materials. *Nat. Rev. Phys.* **5**, 170–184 (2023).
14. Qiu, G. et al. Quantum Hall effect of Weyl fermions in n-type semiconducting tellurene. *Nat. Nanotechnol.* **15**, 585–591 (2020).
15. Zhai, E. et al. The rise of semi-metal electronics. *Nat. Rev. Electr. Eng.* **1**, 497–515 (2024).
16. Chen, J. et al. Topological phase change transistors based on tellurium Weyl semiconductor. *Sci. Adv.* **8**, eabn3837 (2022).
17. Ma, J. et al. Unveiling Weyl-related optical responses in semiconducting tellurium by mid-infrared circular photogalvanic effect. *Nat. Commun.* **13**, 5425 (2022).
18. Ma, Q. et al. Direct optical detection of Weyl fermion chirality in a topological semimetal. *Nat. Phys.* **13**, 842–847 (2017).
19. Cheng, B. et al. Giant nonlinear Hall and wireless rectification effects at room temperature in the elemental semiconductor tellurium. *Nat. Commun.* **15**, 5513 (2024).
20. Dai, M. et al. Long-wave infrared photothermoelectric detectors with ultrahigh polarization sensitivity. *Nat. Commun.* **14**, 3421 (2023).
21. Wang, Y. et al. Field-effect transistors made from solution-grown two-dimensional tellurene. *Nat. Electron.* **1**, 228–236 (2018).
22. Zhao, C. et al. Evaporated tellurium thin films for p-type field-effect transistors and circuits. *Nat. Nanotechnol.* **15**, 53–58 (2020).
23. Blakemore, J. S. & Nomura, K. C. Intrinsic optical absorption in tellurium. *Phys. Rev.* **127**, 1024–1029 (1962).
24. Peng, M. et al. Blackbody-sensitive room-temperature infrared photodetectors based on low-dimensional tellurium grown by chemical vapor deposition. *Sci. Adv.* **7**, eabf7358 (2021).
25. Tsirkin, S. S., Puente, P. A. & Souza, I. Gyrotropic effects in trigonal tellurium studied from first principles. *Phys. Rev. B* **97**, 035158 (2018).
26. Hirayama, M., Okugawa, R., Ishibashi, S., Murakami, S. & Miyake, T. Weyl node and spin texture in trigonal tellurium and selenium. *Phys. Rev. Lett.* **114**, 206401 (2015).
27. Sakano, M. et al. Radial spin texture in elemental tellurium with chiral crystal structure. *Phys. Rev. Lett.* **124**, 136404 (2020).
28. Jnawali, G. et al. Ultrafast photoinduced band splitting and carrier dynamics in chiral tellurium nanosheets. *Nat. Commun.* **11**, 3991 (2020).

29. Zhuo, X. et al. Ultrafast dynamics of photoexcited carriers in tellurium in the vicinity of Weyl nodes. *Phys. Rev. B* **110**, 014311 (2024).
30. Guan, M.-X., Wang, E., You, P.-W., Sun, J.-T. & Meng, S. Manipulating Weyl quasiparticles by orbital-selective photoexcitation in WTe<sub>2</sub>. *Nat. Commun.* **12**, 1885 (2021).
31. Fu, Q. et al. Berry curvature dipole induced giant mid-infrared second-harmonic generation in 2D Weyl semiconductor. *Adv. Mater.* **35**, 2306330 (2023).
32. Tutihasi, S., Roberts, G. G., Keezer, R. C. & Drews, R. E. Optical properties of tellurium in the fundamental absorption region. *Phys. Rev.* **177**, 1143–1150 (1969).
33. Loferski, J. J. Infrared optical properties of single crystals of tellurium. *Phys. Rev.* **93**, 707–716 (1954).
34. Kim, H. et al. Actively variable-spectrum optoelectronics with black phosphorus. *Nature* **596**, 232–237 (2021).
35. Chen, C. et al. Bright mid-infrared photoluminescence from thin-film black phosphorus. *Nano Lett.* **19**, 1488–1493 (2019).
36. Gatti, G. et al. Radial spin texture of the Weyl Fermions in chiral tellurium. *Phys. Rev. Lett.* **125**, 216402 (2020).
37. Chang, G. et al. Topological quantum properties of chiral crystals. *Nat. Mater.* **17**, 978–985 (2018).
38. Nakayama, K. et al. Band splitting and Weyl nodes in trigonal tellurium studied by angle-resolved photoemission spectroscopy and density functional theory. *Phys. Rev. B* **95**, 125204 (2017).
39. Wang, J., Verzhbitskiy, I. & Eda, G. Electroluminescent devices based on 2D semiconducting transition metal dichalcogenides. *Adv. Mater.* **30**, 1802687 (2018).
40. Sze, S. M. *Physics of Semiconductor Devices*. (John Wiley & Sons, 1981).
41. Fox, M. *Optical Properties of Solids*. (Oxford University Press, USA, 2002).
42. Schubert, E. F. *Light Emitting Diodes*. (Cambridge University Press, 2006).
43. Chhajed, S., Xi, Y., Li, Y.-L., Gessmann, T. & Schubert, E. F. Influence of junction temperature on chromaticity and color-rendering properties of trichromatic white-light sources based on light-emitting diodes. *J. Appl. Phys.* **97**, 054506 (2005).
44. Chang, T. Y. et al. Black phosphorus mid-infrared light-emitting diodes integrated with silicon photonic waveguides. *Nano Lett.* **20**, 6824–6830 (2020).
45. Chen, P. L. et al. Van der Waals heterostructure mid-infrared emitters with electrically controllable polarization states and spectral characteristics. *ACS Nano* **17**, 10181–10190 (2023).
46. Tran, V., Fei, R. & Yang, L. Quasiparticle energies, excitons, and optical spectra of few-layer black phosphorus. *2D Mater.* **2**, 044014 (2015).
47. Bie, Y.-Q. et al. A MoTe<sub>2</sub>-based light-emitting diode and photo-detector for silicon photonic integrated circuits. *Nat. Nanotechnol.* **12**, 1124–1129 (2017).
48. Liu, X. et al. Direct linearly polarized emission in van der Waals LEDs via the Flexoelectric effect. *Laser Photonics Rev.* **19**, 2401319 (2025).
49. Krier, A., Sherstnev, V. V., Gao, H. H., Monahov, A. M. & Hill, G. Optical switching in mid-infrared light-emitting diodes. *Appl. Phys. Lett.* **80**, 2821–2823 (2002).
50. Dupont, E., Liu, H. C. & Yang, R. Q. Polarization dependence of electroluminescence in Sb-based mid-infrared interband cascade emitters. *J. Appl. Phys.* **86**, 7195–7197 (1999).
51. Jia, R. et al. Highly efficient inherent linearly polarized electroluminescence from small-molecule organic single crystals. *Adv. Mater.* **35**, 2208789 (2023).
52. Ye, J. et al. Direct linearly polarized electroluminescence from perovskite nanoplatelet superlattices. *Nat. Photonics* **18**, 586–594 (2024).
53. Pradhan, S. et al. High-efficiency colloidal quantum dot infrared light-emitting diodes via engineering at the supra-nanocrystalline level. *Nat. Nanotechnol.* **14**, 72–79 (2019).
54. Tong, L. et al. Stable mid-infrared polarization imaging based on quasi-2D tellurium at room temperature. *Nat. Commun.* **11**, 2308 (2020).
55. Hasan, M. Z. et al. Weyl, Dirac and high-fold chiral fermions in topological quantum matter. *Nat. Rev. Mater.* **6**, 784–803 (2021).

## Acknowledgments

This work was supported by the National Key R&D Program of China, grant No. 2021YFA1200804 (K.Z.), National Natural Science Foundation of China grant No. 62274175 (J.W.), T2325025 (K.Z.), Major Science and Technology Special Project of Jiangsu Province grant BG2024017 (J.W.), Jiangsu Province Key R&D Program grant No. BK20232044 (K.Z.), Suzhou Basic Research Program grant No. SJC2023004 (K.Z.), and the China Postdoctoral Science Foundation under Grant Number 2025M770194 (J.Z.). J.W. acknowledges the support from the Gusu Leading Talents Program (ZXL2023166) and the CAS Young Talent program. F.X. thanks the Basic Research Program of Jiangsu Province (Grants No. BK20240395). Calculations were performed on Sugon HPC clusters equipped with HYGON X86 32-core processors (2.5 GHz). The authors are grateful for the technical support for the Vacuum Interconnected Nanotech Workstation (Nano-X) from Suzhou Institute of Nano-Tech and Nano-Bionics (SINANO), Chinese Academy of Sciences.

## Author contributions

K.Z. and J.W. conceived and supervised the project. The Te nanosheets were synthesized by J.Z., Q.H., and K.C.; J.Z. and Junsheng X. fabricated Te-based heterostructure devices and performed optical characterization of LED devices with assistance from Y.L., Q.Z., and Jing X.; Crystallographic characterization of Te was performed by X.H., assisted by X.W.; First-principles calculation was done by F.X. and J.S.; D.W. drew the schematic diagram. Y.G. and X.Y. provided the simulation of the Te heterostructure device. B.R. and W.Z. provided micro-resolution pump-probe reflectance spectroscopy measurements. All authors contributed to the data analysis. J.Z., J.S., F.X., and J.W. wrote the paper with input from all authors.

## Competing interests

The authors declare no competing interests.

## Additional information

**Supplementary information** The online version contains supplementary material available at <https://doi.org/10.1038/s41467-025-66014-1>.

**Correspondence** and requests for materials should be addressed to Junyong Wang or Kai Zhang.

**Peer review information** *Nature Communications* thanks the anonymous reviewers for their contribution to the peer review of this work. A peer review file is available.

**Reprints and permissions information** is available at <http://www.nature.com/reprints>

**Publisher's note** Springer Nature remains neutral with regard to jurisdictional claims in published maps and institutional affiliations.

**Open Access** This article is licensed under a Creative Commons Attribution-NonCommercial-NoDerivatives 4.0 International License, which permits any non-commercial use, sharing, distribution and reproduction in any medium or format, as long as you give appropriate credit to the original author(s) and the source, provide a link to the Creative Commons licence, and indicate if you modified the licensed material. You do not have permission under this licence to share adapted material derived from this article or parts of it. The images or other third party material in this article are included in the article's Creative Commons licence, unless indicated otherwise in a credit line to the material. If material is not included in the article's Creative Commons licence and your intended use is not permitted by statutory regulation or exceeds the permitted use, you will need to obtain permission directly from the copyright holder. To view a copy of this licence, visit <http://creativecommons.org/licenses/by-nc-nd/4.0/>.

© The Author(s) 2025